Cationic and anionic dual redox activity of MoS_2 for electrochemical potassium storage

Ajay Piriya Vijaya Kumar Saroja,[1] Yupei Han,[1] Charlie AF Nason,[1] Gopinathan Sankar,[1] Yi Lu,[1] Henry R Tinker,[1] Andrew Stewart,[1] Veronica Celorrio,[2] Min Zhou,[3] Jiayan Luo,[4] Yang Xu[1,*]

[1]Department of Chemistry, University College London, London WC1H 0AJ, UK

[2]Diamond Light Source, Harwell Science and Innovation Campus, Didcot OX11 0DE, UK

[3] Hefei National Research Center for Physical Sciences at the Microscale, School of Chemistry and Materials Science, University of Science and Technology of China, Hefei, Anhui 230026, China

[4]State Key Laboratory of Metal Matrix Composites, School of Materials Science and Engineering, Shanghai Jiao Tong University, Shanghai 200240, China

Corresponding author: Yang Xu (y.xu.1@ucl.ac.uk)

Abstract

MoS_2 is receiving intensive attention in the research area of potassium-ion batteries (PIBs) and regarded as one of the most promising PIB anodes. Great progress has been made to enhance the electrochemical performance of MoS_2, but understanding of the electrochemical mechanism to store K-ion in MoS_2 remains unclear. This work reports that the K storage process in MoS_2 follows a complex reaction pathway involving the conversion reactions of both Mo and S and as a result, the storage process shows both cationic redox activity of Mo and anionic redox activity of S. The presence of dual redox activity, characterized in-depth through synchrotron X-ray absorption, X-ray photoelectron, Raman, and UV-vis spectroscopies, reveals the irreversible Mo oxidation during the depotassiation process redirects the reaction pathway towards S oxidation, which leads to the progression of K-S electrochemistry in the (de)potassiation process. Moreover, the dual reaction pathway can be regulated by controlling the discharge depth at different cycling stages of MoS_2, realizing a long-term stable cycle life of MoS_2 as a PIB anode.

Keywords: metal chalcogenide, conversion reaction, polysulfides, layered structure, anionic redox, potassium-ion battery, potassium-sulfur battery

1. Introduction

Two-dimensional transition metal dichalcogenides (2D TMDs) are fundamentally fascinating and chemically versatile materials for a variety of applications.[1,2] Among various TMDs, molybdenum disulfide (MoS_2) has been intensively investigated due to its extraordinary intrinsic properties such as high optical absorption, active catalytic sites, high Young's modulus and Seebeck coefficient. These properties have made MoS_2 highly desirable in many research domains including heterojunction solar cells,[3,4] electro/photocatalysis,[5,6] strain sensors[7] and thermoelectric devices.[8] Particularly, the layered structure composed of S-Mo-S slabs provides highly accessible sites, resulting in MoS_2 being a promising electrode material for battery applications.[9–12] In the area of potassium-ion batteries (PIBs) where the large size of K-ion poses a major challenge for electrode materials discovery, the wide interlayer spacing (0.62 nm) and weak Van der Waals interaction between the S-Mo-S slabs can effectively accommodate K-ions and lower the energy barrier of K-ion diffusion. The capability to transfer up to four electrons per MoS_2 formula indicates a high theoretical capacity (670 mAh g^{-1}). These advantages have made MoS_2 one of the most studied anode materials of PIBs.[10,13–15]

A great deal of research attention has been directed towards enhancing the PIB performance of MoS_2 by addressing issues such as poor electronic conductivity and structural instability. Carbon coating[16–18] and phase engineering (1T phase and 1T/2H mixed phase)[19–22] can improve electron transfer owing to the presence of carbon and the metallic nature of the 1T phase (10-100 S cm^{-1}),[23] respectively. Structural stability can be strengthened by expanding interlayer spacing [24–26] and tuning the morphology and/or dimensionality of MoS_2 to relieve the strain in vertical and radial directions during K-ion insertion.[27,28] While progress has been made to driving the PIB performance development of MoS_2, understanding of the electrochemical mechanism to store K-ions has not been progressed to the same extent as performance development, due to the complexity in phase transition and kinetic processes involved in electrochemical K storage in MoS_2.[27,29–31] Understanding the mechanism is crucial to guide the structural and phase engineering of MoS_2 and even intrigue new design strategies.

Electrochemical storage mechanism of alkali-ions in MoS_2 is strongly affected by the thermodynamic formation energy and polarity of alkali-metal-sulfur bond. This could result in different mechanisms between K storage and Li/Na storage in MoS_2 because K-S bond has a lower formation energy and less polar nature than Li-S and Na-S bonds. Even comparing Li and Na storage in MoS_2, the mechanisms reported in literature varied from study to study and diverse conclusions were drawn. It has been reported that MoS_2 was regenerated after delithiation, accompanied by the structural transition from bulk to nanostructures.[32] However, the regeneration was not observed in other studies, instead partially reversible conversion reaction back to MoS_2[33] and even irreversible conversion reaction[34] were observed in Li. Sodiation in MoS_2 was reported to be a reversible[35,36] and an irreversible[37] conversion process with the structure changing to few layers. Another study[38] reported MoS_2 failed to undergo conversion reaction; instead, sodiation caused structural transition forming distorted MoS_x clusters, with partial regeneration to MoS_2 after desodiation. In the case of K storage, there have been very limited studies, but yet vastly different results were seen. Du et al. reported K-ion favoured intercalating in MoS_2 to form $KMoS_2$ and the reversible reaction between $KMoS_2$ and K_xMoS_2 was limited only to an intercalation process, being responsible for K storage.[39] However, other studies reported a range of discharge products including K_2S[40] and a mixture of K_xMoS_2, K_2S_5 and K_2S,[13,41] suggesting K-ion storage in MoS_2 might undergo a more complex mechanism than the Li and Na counterparts. Note that the kinetics of K-ion diffusion in MoS_2 is sluggish due to the large size of K-ion, and this can further increase the complexity of K-ion storage mechanism.

In this work, we investigated the mechanism of K storage process in MoS_2 using commercially available material and a combination of electrochemical, spectroscopic, structural, and morphological characterizations. We unrevealed the formation of metallic Mo and molecular S at the depotassiated state of MoS_2, which is due to the irreversible oxidation of the metallic Mo formed at the potassiated state to Mo^{4+} and the resulting oxidation of S^{2-} to S^0. As a result, a dual reaction pathway enabled by Mo cationic redox activity and S anionic redox activity (i.e., K-S electrochemistry) directed the K storage process in MoS_2. Moreover, the combined characterizations showed the effect of the dual reaction pathway on the PIB performance of MoS_2, based on which we provided a solution of controlling discharge depth at different cycling stages, i.e., deep discharge at 0.001 V in the 1st cycle and raising discharge depth to 0.2 V from the 2nd cycle, to realize high cycling stability and rate capability. Using the solution, the MoS_2 electrode was able to deliver a stable capacity retention of 84% after 500 cycles and capacities of 121 and 91 mAh g^{-1} at 1 and 2 A g^{-1}, respectively. To the best of our knowledge, this is the first comprehensive investigation on the K storage mechanism of MoS_2. Unlike the mainstream study of MoS_2 for PIBs, our investigation reveals interesting simultaneous cationic and anionic redox activity of the material, contributing new insights into design strategies to further enhance the PIB performance of MoS_2, for instance, developing strategies to reduce the dissolution of polysulfides, integrate catalysts to enhance sulfur redox activity, and incorporate secondary component to regulate the distribution of Mo and S redox reaction products.

2. Experimental section

2.1 Materials

Commercial MoS_2 was purchased (product number 6694710, BDS chemicals Ltd England) and used as received.

2.2 Materials characterization

The crystal structure of MoS_2 was characterized using STOE SEIFERT X-ray diffractometer with Cu Kα source (1.5406 Å, 40 kV, 30 mA). The surface morphology and lattice spacing of MoS_2 were observed by scanning electron microscope (SEM, JEOL JSM 7600) and transmission electron microscope (TEM, JOEL-2100), respectively. Raman spectra were recorded with RENISHAW Raman spectrometer system using 633 nm laser. The chemical states of S and Mo in MoS_2 were evaluated by X-ray photoelectron spectrometer (XPS, Thermo Scientific K-alpha photoelectron spectroscopy) with Al K-α (1486.6 eV) as the X-ray source. The binding energy was calibrated using C_{1s} at 284.8 eV. Data analysis of XPS results was carried out using CasaXPS and high-resolution peaks were deconvoluted using Gaussian-Lorentzian function. UV-vis spectra of the discharged electrodes were measured using UV-Vis spectrophotometer (Shimadzu, UV 2600) in the wavelength range of 200 to 800 nm. The X-ray absorption near edge structure (XANES) spectroscopy measurements of MoS_2 electrodes were carried out at B18 beamline of Diamond Light Source, UK. The Mo K-edge of all the samples were sealed in an aluminum pouch case inside a glove box preventing exposure to air. Mo K-edge spectra were recorded in transmission mode at room temperature. For the post analysis studies, the cycled cells were disassembled in an argon filled glove box and the electrodes were washed with propylene carbonate and dried in the glove box.

2.3 Electrochemical measurements

MoS_2 electrodes were prepared by mixing 75 wt.% MoS_2, 10 wt.% super P as the conducting agent and 15 wt.% sodium carboxyl methyl cellulose as the binder in DI water to form a slurry. The slurry mixture was coated on a copper foil (9 µm thickness) and dried under vacuum at 60 ˚C overnight. The dried electrodes were punched in the form of discs (diameter 12 mm) and the loading of the active material was 1.5-2 mg cm^{-2}. CR 2032 coin cells were assembled in an argon filled glove box (O_2 < 0.5 ppm, H_2O < 0.5 ppm) using glass fiber B (Whatman Glass Microfiber Filters) as the separator and potassium metal (98%, Thermo Fisher) as the counter and reference electrode. 1 M bis(fluorosulfonyl)imide potassium salt (KFSI) dissolved in 1:1 volume ratio of ethylene carbonate (EC) and diethyl carbonate (DEC) was used as the electrolyte. Galvanostatic charge discharge (GCD) measurements were tested in NEWARE battery cyclers (5V, 20 mA). Cyclic voltammetry (CV) measurements were tested in Biologic VSP potentiostat. Coin cells were rested for 12 h before electrochemical measurements were carried out under different potential ranges including 0.2-2.5 V and 0.001-2.5 V (vs. K^+/K) at various current densities and scan rates.

4. Results and discussions

The XRD pattern of commercial MoS_2 (Figure S1a) shows the characteristic diffraction peaks of 2H MoS_2 (98-003-9095) with high crystallinity. Raman spectrum (Figure S1b) shows peaks appearing at 383 and 407 cm^{-1} corresponding to in-plane Mo-S phonon mode (E^1_{2g}) and out of plane Mo-S (A_{1g}) vibrational modes, respectively, further demonstrating the 2H phase.[40] In addition, the peak located at 464 cm^{-1} corresponds to the combination of two Longitudinal Acoustic (LA) modes caused by the resonance of excitation wavelength.[42] The other peaks represent the combination of LA modes and E^1_{2g}/A_{1g} modes.[42,43] To reveal the chemical state of MoS_2, high resolution XPS spectra of Mo 3d and S 2p were deconvoluted. The Mo 3d spectra (Figure S1c) show a main doublet of Mo $3d_{5/2}$ and Mo $3d_{3/2}$ at the binding energies of 232.2 and 229.1 eV, demonstrating the Mo^{4+} state.[13,44] The weak doublet at 233.2 and 235.6 eV suggests slight surface oxidation to Mo^{6+}.[30,45] The presence of S^{2-} in MoS_2 (Figure S1d) is confirmed by the doublet of S $2p_{3/2}$ and S $2p_{1/2}$ peaks at 162.8 and 163.9 eV, respectively.[44] SEM images (Figures S1e and S1f) show a layered sheet-like morphology with an average lateral size of ~30 µm and a thickness of ~5 µm. Moreover, the high resolution TEM (HRTEM) image (Figure S1e inset) clearly shows the presence of stacked multilayers with a lattice spacing of 0.62 nm which agrees well with the (002) lattice spacing of 2H MoS_2.[46] The elemental mapping of MoS_2 shows homogeneous distribution of Mo and S with no impurities and a Mo: S ratio of 1:2.2 (Figure S2).

We first investigated the GCD profiles of the MoS_2 electrodes cycled in the range of 0.001 to 2.5 V (denoted as Route A in Figure 1a) in the half-cell configuration, as this has been the voltage range (i.e., deep discharge) used in the literature to study MoS_2 as an anode material of PIBs. As shown in Figure S3a, the first discharge curve exhibited three voltage plateaus, suggesting a multi-step potassiation process. XRD patterns (Figure S3b) were obtained for the discharge products at the end of each voltage plateau (stage II: discharge to 0.5 V, stage III: discharge to 0.2 V, and stage IV: discharge to 0.001 V, shown in Figure S3a). At stage II, the (002) peak was broadened and a new peak at 8.9° appeared, which indicates the initial K-ion intercalation retains the layered structure but expands the interlayer spacing, forming an intermediate phase K_xMoS_2 (x = ~0.4).[47] Further discharging to stage III caused more K-ion intercalation, as evidenced by the increase in peak intensity at 8.9° and near disappearance of the original (002) peak. From stage III to IV, a long and stable voltage plateau appeared at ~0.1 V and both peaks at 14.3° and 8.9°, which signals the presence of the layered structure, diminished, while a broad peak appeared at 13.4°. This indicates the layered structure was destroyed and amorphous products formed at the deep discharge condition. At the end of the following charge (stage V), no crystalline product(s) can be detected in the XRD pattern, suggesting there was minimal to no restoration of the pristine multi-layered structure of MoS_2. The observations of the GCD profiles via Route A (0.001-2.5 V) directed our attention to the control of discharge depth and its effect on K storage mechanism in MoS_2. Since the layered structure was retained at >0.2 V potassiation and amorphous discharge products were formed at <0.2 V potassiation, we kept the discharge depth at 0.001 V in the 1st cycle but changed it to 0.2 V from the 2nd cycle and onwards (denoted as Route B: 0.001-2.5 V in the 1st cycle and 0.2-2.5 V from the 2nd cycle in Figure 1b). Figure 1b shows the GCD profiles via Route B and the XRD patterns of the MoS_2 electrodes at various stages of the cycles are shown in Figure S4. The GCD profiles share similarities with those via Route A, including the three defined plateau regions in the first discharge curve and the sloping curves in the following cycles. The similarities can also be seen from the CV curves via the two routes (Figure S5), showing similar voltages of reduction and oxidation peaks. No crystalline phase(s) was recovered via Route B and (de)potassiation product(s) remained amorphous judging from the XRD patterns.

However, we found that the two routes resulted in surprisingly different cell performance. First, cycle1 charge and cycle2 discharge capacities via route B were 393 and 273 mAh g^{-1}, respectively, at 20 mA g^{-1}, being close to the corresponding capacity via route A (318 and 279 mAh g^{-1}). It is not difficult to understand cycle1 charge capacity being close, as the two routes underwent the same deep discharge process during the 1st cycle. However, the similar cycle2 discharge capacity suggests there was extra capacity generated in the 0.2-2.5 V range via Route B to compensate for the capacity loss that would have been gained in the 0.001-0.2 V range via Route A. Second, despite the smaller voltage range from cycle2 onwards, Route B resulted in higher capacities than Route A across all current densities tested for rate capability (Figure 1c). The cell via Route B delivered capacities of 256, 236, 222, 198, 160, 134, 124, and 91 mAh g^{-1} at 30, 50, 100, 200, 500, 800, 1000, and 2000 mA g^{-1}, respectively. It retained 263 mAh g^{-1} when returning to 30 mA g^{-1}. In contrast, the cell via Route A showed rapid capacity decay and failed at >1 A g^{-1}. Third, Route B exhibited much better cycling stability than Route A (Figure 1d). At 100 mA g^{-1}, the cell via Route B delivered an initial discapacity of 167 mAh g^{-1}, 77% of which was retained after 200 cycles. Although the cell via Route A delivered a higher capacity in the initial cycles due to the wider voltage range (0.001-2.5 V), only 54%

capacity was retained after 200 cycles, being surpassed by the cell via Route B from cycle154 onwards. The same trend was observed at 1 A g^{-1} over 500 cycles (Figure 1e). Route B resulted in 84% capacity retention in comparison to 44% retention via Route A. We are mindful that the PIB performance obtained here is not comparable to some of the best in literature obtained by forming nanocomposites[31,48] because commercial MoS_2 in a bulky size was directly used in our work. However, the comparison of the two routes shown here is intriguing in the sense that despite the smaller voltage range of Route B than Route A from cycle2 onwards, the former exhibited better rate capability, more stable cycle life, and high capacity over long-term cycling. This indicates K storage in MoS_2 may undergo a more complex process than what has been reported in literature, i.e., an intercalation reaction followed by a conversion reaction (possible overlap depending on sample status). Additional reaction(s) may occur simultaneously, and controlling discharge depth can affect the additional reaction(s), thus affecting the PIB performance of MoS_2.

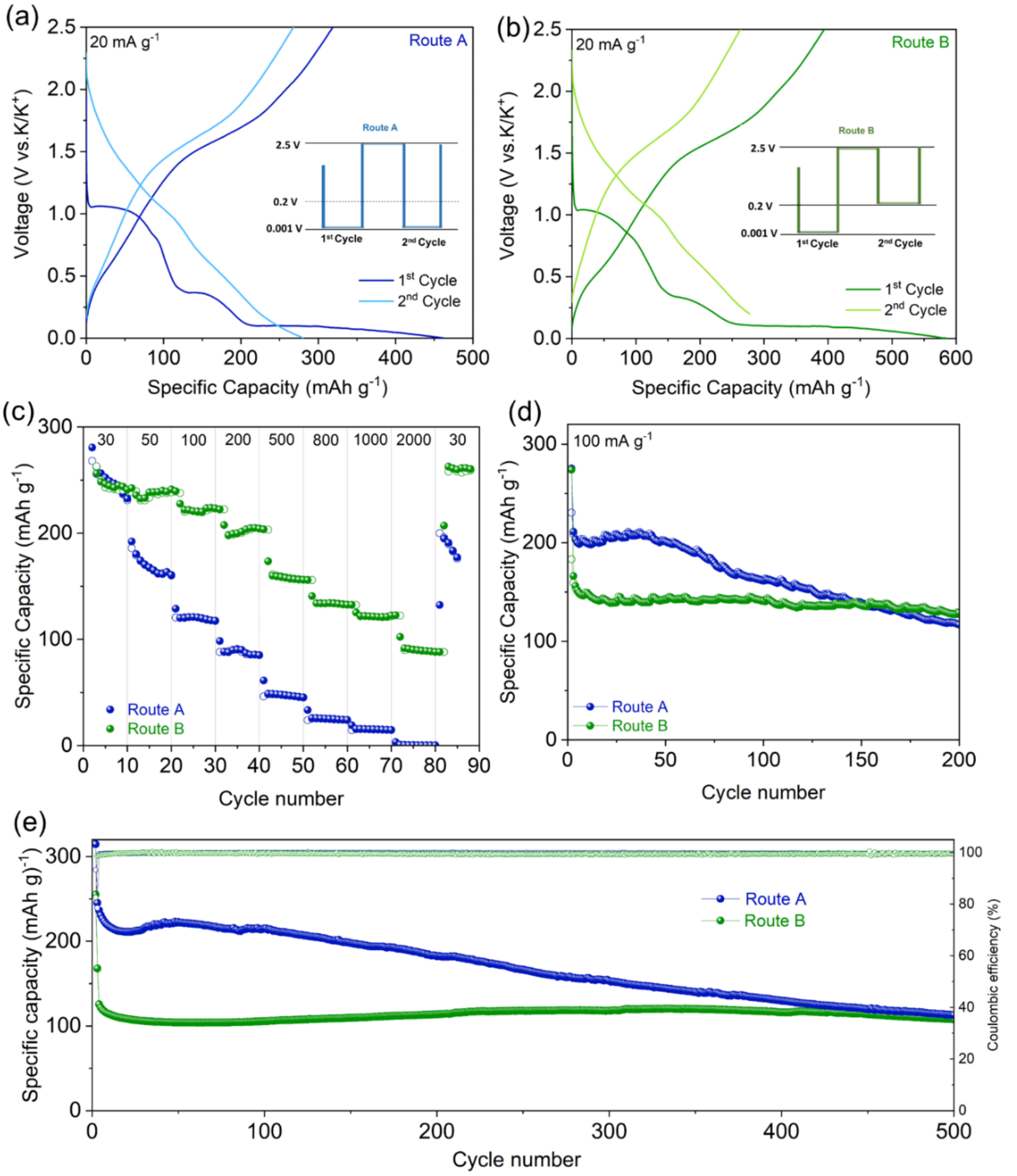

Figure 1. GCD profiles of MoS_2 via Route A (a) and Route B (b). Comparison of rate capability (c) and cycle stability at 100 mA g^{-1} (d) and 1 A g^{-1} (e) of MoS_2 cycled via the two routes.

We then turned our focus to investigate the change of Mo and S, the two elements in MoS_2, during the cycles. We combined various spectroscopy techniques including XAS, XPS, Raman and UV-vis spectroscopies for the investigation due to the amorphous nature of the discharge and charge products as shown in the previous discussion. The local structural change of the Mo species in MoS_2 in the first two cycles via Route B was characterized using EXAFS spectra

(Figure 2a). Figure 2a shows the Fourier transformed (FT) Mo K-edge EXAFS taken at various states during the first two cycles via Route B. The fitting of the EXAFS spectra is shown in Figure S6. Two strong peaks can be seen at 2.4 Å and 3.1 Å from pristine MoS_2, representing the Mo-S interaction in the 1st coordination shell and the Mo-Mo interaction in 2nd coordination shell of 2H- MoS_2, respectively (Figure 2a).[49] When discharged to 0.2 V, the Mo-Mo (3.1 Å) peak of MoS_2 decreased and the decrease in intensity was caused by structural transformation of MoS_2 to K_xMoS_2.[33] Further potassiation to 0.001 V caused a significant decline of the amplitude of the Mo-S peak and a strong amplitude of the Mo-Mo interaction at 2.8 Å, the latter corresponding to metallic Mo seen in the Mo foil reference. This proves the occurrence of the conversion reaction that results in the loss of layered structure and the reduction of Mo^{4+} to Mo^0.[33] At the end of the 1st charge, Mo-S peak was resumed as expected due to the restoration of the MoS_2 structure upon depotassiation, but not to the same extent of pristine state. Interestingly, the Mo-Mo peak was present alongside with the Mo-S peak and with a similar amplitude, which clearly suggests the partial oxidation of Mo^0 back to Mo^4[50,51] and the coexistence of metallic Mo with the restored MoS_2. The next cycle in the 0.2-2.5 V range showed reversible peak changes, where Mo-S decreased upon potassiation and increased upon depotassiation, whereas Mo-Mo was present throughout (de)potassiation and became even stronger than Mo-S after the 2nd depotassiation. The best-fit results of coordination number (CN) are provided in Table S1. The CN of Mo-S bond decreased during discharge, signifying the structural transformation of MoS_2. In addition, the presence of metallic Mo upon depotassiation was proven by the Mo 3d XPS spectra. As shown in Figure 2b, the Mo^0 peaks can be seen at 228.9 ($3d_{3/2}$) and 226.1 eV ($3d_{5/2}$) at the end of the 1st and 2nd charge, together with Mo^{4+} from the reverse conversion reaction and $Mo^{5+/6+}$ due to partial surface oxidation of the XPS samples. Furthermore, metallic Mo at the depotassiated state of MoS_2 can be detected even after long-term cycles. As shown in Figures 2c and S7, dense particles with an average size of 1.5 nm distributed throughout the MoS_2 layers. The particles can be characterized to Mo nanocrystals from the selected area electron diffraction (SAED) pattern that shows diffraction spots indexed to the (011) planes of MoS_2 (ICSD: 98-003-9095) and the (011) and (002) planes of Mo (ICSD: 98-005-1508), confirming the coexistence of MoS_2 and Mo in the charged state after cycling. In the case of Route A, we also observed the coexistence of metallic Mo^0 and Mo^{4+} upon depotassiation (Figure S8). Based on these results, it is safe to say that the reverse conversion from Mo^0 to Mo^{4+} during depotassiation was incomplete and metallic Mo was present throughout the cycles. However, the consistent presence of metallic Mo would reduce the electrochemically active species in the electrode, and thus there must be other species that are electrochemically active to contribute to electron transfer and eventually capacity. This prompted us to investigate the change of S.

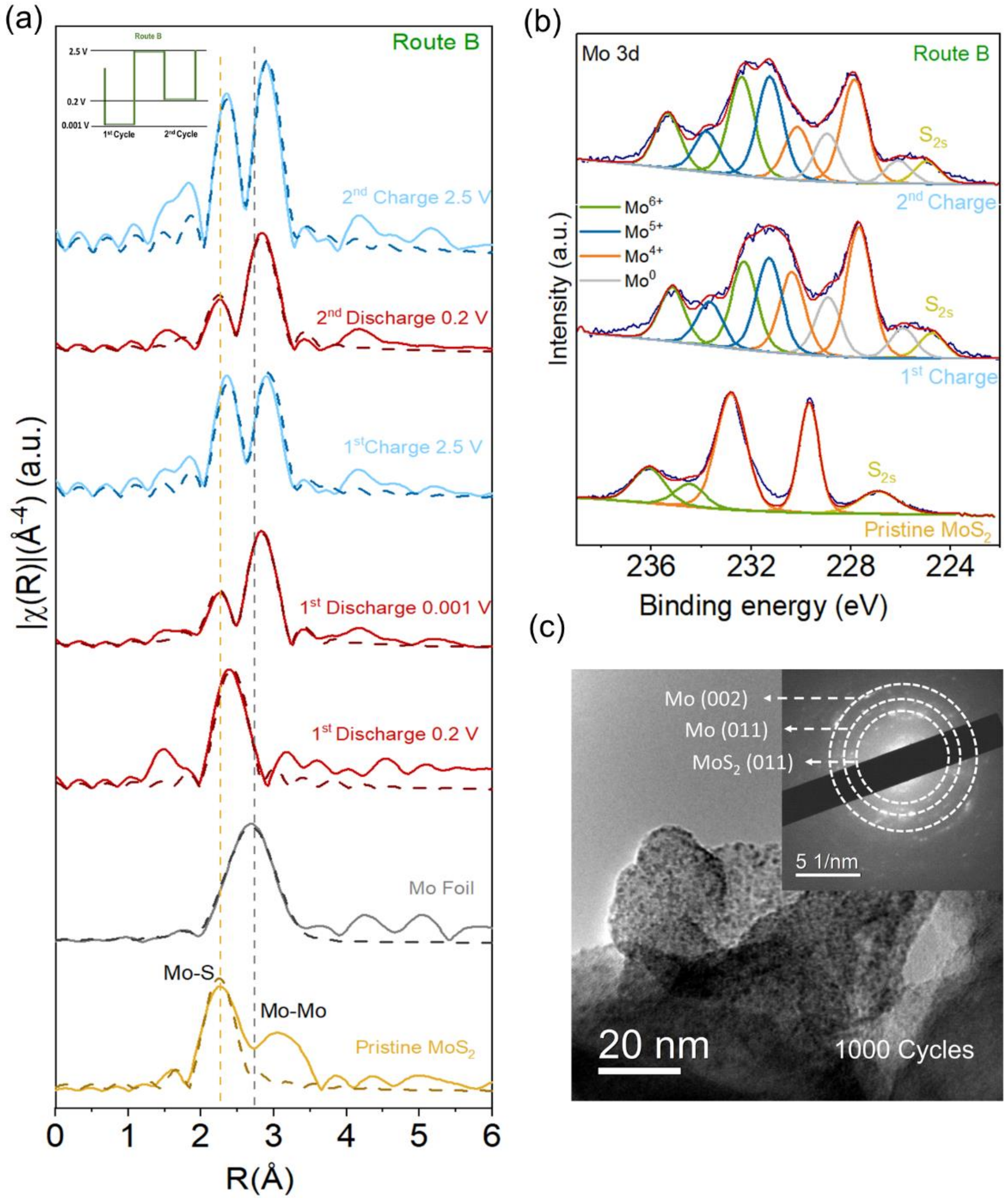

Figure 2. (a) EXAFS spectra of MoS_2 cycled via Route B during the 1st and 2nd discharge/charge process. (b) Mo 3d XPS spectra of MoS_2 cycled via Route B in the charged states. (c) TEM image of MoS_2 cycled via Route B at the charged state (c, inset: SAED pattern).

Figure 3 shows the change of the S species in MoS_2 in the first 2 cycles via Route B. Note that KFSI was replaced by KPF_6 as the salt in the electrolyte to avoid the interference of the S species in KFSI for the interpretation of the results. The S 2p XPS spectra in the 1st cycle are shown in Figure 3a. It shows various potassium polysulfides at the discharged state (potassiation), which agrees with previous work.[52,53] Particularly, the presence of S^{2-}, evidenced by the peaks at 160.1 and 158.7 eV, signals the formation of K_2S and the reduction of Mo^{4+}.[52] What is interesting is that, after depotassiation, peaks of S^0 appeared at 163.2 and 164.8 eV,[54,55] and the peak area of S_3^{2-}/S_x^{2-} increased at the expense of the decrease in S_2^{2-}/S^2. The same changes of the S species were observed in the 2nd cycle (Figure 3b) but with stronger S^0 peak intensity. This suggests during depotassiation, S species was oxidized alongside the partial oxidation of metallic Mo, leading to the formation of S^0 after charge, which essentially contributes to electron transfer and thus capacity. To ascertain our results, we tested the Raman spectra of the MoS_2 electrodes at charged states (depotassiation) in the 1st and 2nd cycles. As shown in Figure 3c, compared to pristine MoS_2, the signature E^1_{2g} and A_{1g} vibrational modes largely diminished, signaling the partial restoration of pristine MoS_2. New peaks evolved at 155 and 244 cm^{-1} in both cycles, corresponding to the torsion and bending vibration modes of sulfur (S_8)[56] and therefore further proving the formation of S^0 after depotassiation. Our analysis of the S species in MoS_2 points to the fact that, beside Mo, S was electrochemically active after the first potassiation and participated in the oxidation and reduction reactions in the following cycles, effectively making K-S chemistry a part of the K storage mechanism in MoS_2; in another word, the mechanism is based on both Mo cationic redox and S anionic redox activities. As known, the S conversion process involved in K-S chemistry can lead to the formation of both low-order polysulfides and high-order polysulfides, the latter of which are in the liquid form and can dissolve in electrolytes.[57,58] If K-S chemistry were to take part in the K storage in MoS_2, we would see high-order polysulfides formed during potassiation dissolving in the electrolyte; as expected, we detected the absorption peaks of S_6^{2-} and S_5^{2-} at 300 and 318 nm,[55,57] respectively, in the UV-vis absorption spectrum of the electrolyte extracted from the separator after the 2nd discharge (Figure 3d). In the case of Route A, since the discharge depth was kept at 0.001 V in all cycles, it is expected that Mo cationic redox and

S anionic redox should both contribute to K storage and the extent to which S anionic redox contributes should be higher than Route B, because deeper discharge depth (0.001 vs. 0.2 V) could promote more Mo reduction and as a result, more irreversible Mo oxidation and more S oxidation. As shown in Figure S9, S^0 was observed after the 1st and 2nd charge in the XPS (Figures S9a and S9b) and Raman spectra (Figure S9c), with more noticeable signals after the 2nd charge compared to Route B. Also, S_6^{2-} and S_5^{2-} absorption peaks were observed in the UV-vis absorption spectrum (Figure S9d).

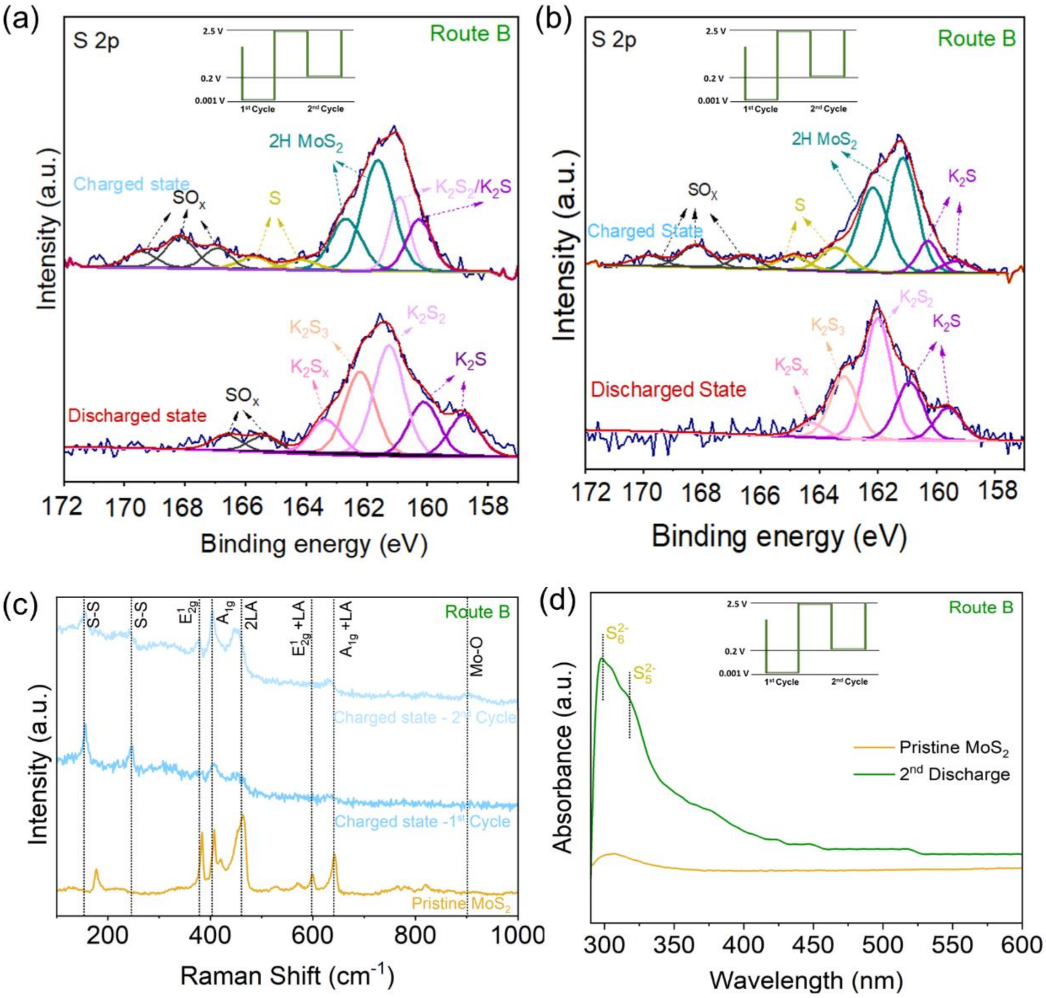

Figure 3. S 2p XPS spectra of MoS_2 via Route B in the 1st (a) and 2nd cycles (b). (c) Raman spectra of MoS_2 cycled via Route B in the charged states. (d) UV-vis absorption spectra of the electrolyte cycled via Route B in the discharged state of MoS_2.

Our next characterization was to show the cationic and anionic dual redox activity can sustain over repeated cycles for the K storage in MoS_2. As shown in Figure 4a, high-order polysulfides S_6^{2-} and S_5^{2-} were observed at 245 and 297 nm, respectively, in the UV-vis absorption spectrum after 20 cycles for both Route A and Route B. In the Raman spectra shown in Figure 4b, the presence of the torsion and bending vibration modes of S^0 proves the reversible transformation of polysulfides to sulfur at the charged state for both routes. Combing the HRTEM results shown in Figures 2c, where Mo^0 was detected at the charged state, the collective results demonstrate the active cationic and anionic dual redox reactions can sustain over repeated cycles, forming dual reaction pathways of the K storage in MoS_2.

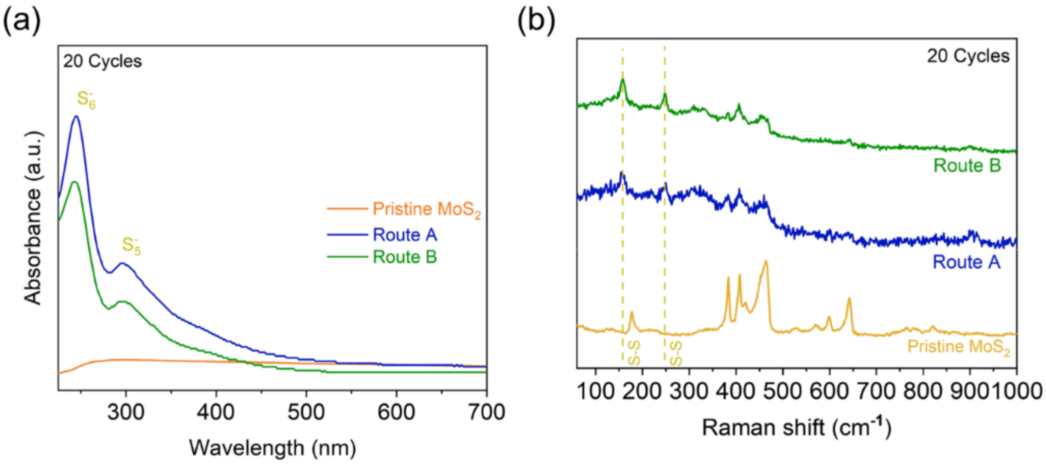

Figure 4. (a) UV-vis absorption spectra of the electrolytes cycled via Routes A and B in the discharged state of MoS_2 after 20 cycles. (b) Raman spectra of MoS_2 cycled via Routes A and B in the charged states after 20 cycles.

Furthermore, we pointed out in the previous discussion that multiple reactions may occur during K storage in MoS_2 and controlling discharge depth could affect the reactions and thus the PIB performance of MoS_2. Building on our results of cationic and anionic dual redox activity, we carried out post-cycling morphological and structural characterizations to understand how controlling discharge depth, the main difference between Route A and Route

B, affects the dual reaction pathways and the resulting performance. Constant cycling in the 0.001-2.5 V range (Route A) can maximize capacity because it maximizes the conversion reaction of the Mo species, i.e., cationic redox activity, and potentially maximizes the formation of S^0, i.e., anionic activity, due to the increasingly irreversible Mo oxidation. This was reflected by the high capacity shown in Figure 1. However, this could result in three consequences: (i) repeatedly destroying the MoS_2 layered structure at deep discharge depth and reconstructing the structure during charge, (ii) accumulating irreversible discharge products, and (iii) increasing S^0 formation and polysulfide dissolution in the electrolyte, all of which are responsible for the capacity decay and deteriorated rate capability via Route A. SEM images (Figures 5a and S10a) show large agglomerations and cracks formed after 1000 cycles, signaling a much thickened (presumably due to continuous formation of solid-electrolyte interphase (SEI)) and stiff surface of the electrode. TEM image (Figure 5b) shows the total collapse of the pristine layered structure (Figure S1e), likely increasing K-ion interparticle diffusion resistance. In contrast, discharging to 0.001 V in cycle1 and raising the discharge depth to 0.2 V from cycle2 (Route B) can balance between maximizing dual cationic and anionic redox activity and minimizing surface deterioration and structural collapse, because the dual redox activity is activated in cycle1 and at the same time, the MoS_2 structure is less prone to collapse from cycle2 after the extent to which the conversion reaction takes place is reduced. The electrode after 1000 cycles (Figures 5c and S10b) show a much smoother surface with more defined texture and without cracks via Route B compared to Route A. Layered structure was retained with expanded interlayer spacings (Figure 5d). Additionally, metallic Mo nanoclusters might act as active sies to bind polysulfides and hinder the shuttle effect.[34,59–61] Collectively, these contributing factors enable long-term cycling stability and rate capability via Route B. Therefore, utilizing cationic and anionic dual redox activity can be advantageous for storing K in MoS_2, but the execution of it needs to be balanced.

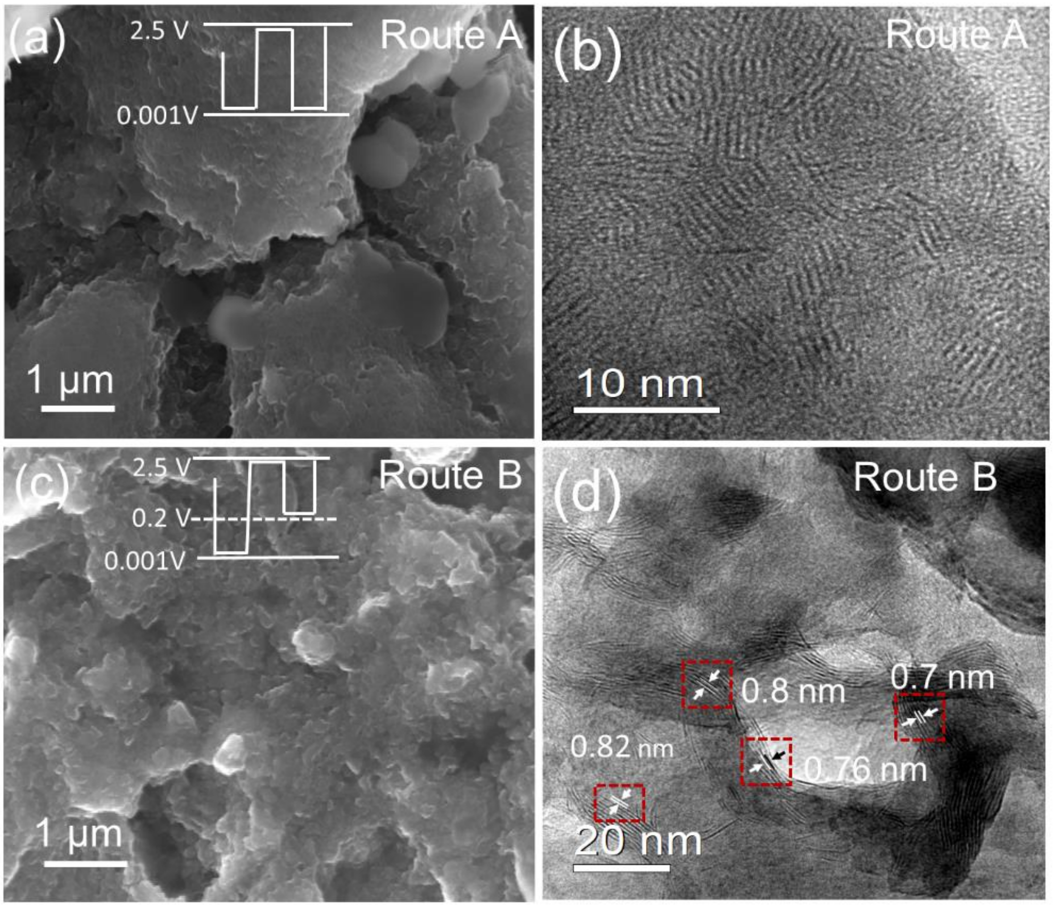

Figure 5. SEM (a and c) and TEM images (b and d) of the MoS_2 electrodes cycled via Route A (a and b) and Route B (c and d) after 1000 cycles.

With the above results and discussion, we illustrate in Figure 6 the K storage mechanism in MoS_2. The initial potassiation process at the discharge depth of 0.001 V undergoes a conversion reaction to form a mixture of discharged products including metallic Mo nanoclusters, potassium (poly)sulfides, and potassium intercalated MoS_2 (K_xMoS_2). The subsequent depotassiation process up to 2.5 V does not completely oxidize metallic Mo to higher oxidation states and a part of metallic Mo remains, which results in a part of potassium sulfides being oxidized to S^0. In the following cycles, a dual reaction pathway consisting of Mo cationic redox activity and S anionic redox activity takes place, enabling the capacity contribution from transition metal Mo and K-S battery chemistry. Via Route A with which discharge depth is kept at 0.001 V, the MoS_2 layered structure is destroyed over cycles and polysulfide dissolution in the electrolyte is increased, leading to fast capacity decay and unstable cyclability. Via Route B with which discharge depth is kept at 0.2 V from cycle2 onwards, severe MoS_2 structural deterioration is avoided over cycles and polysulfide dissolution in the electrolyte is reduced, enabling stable cyclability and good rate capability without losing the dual cationic anionic redox reactivity.

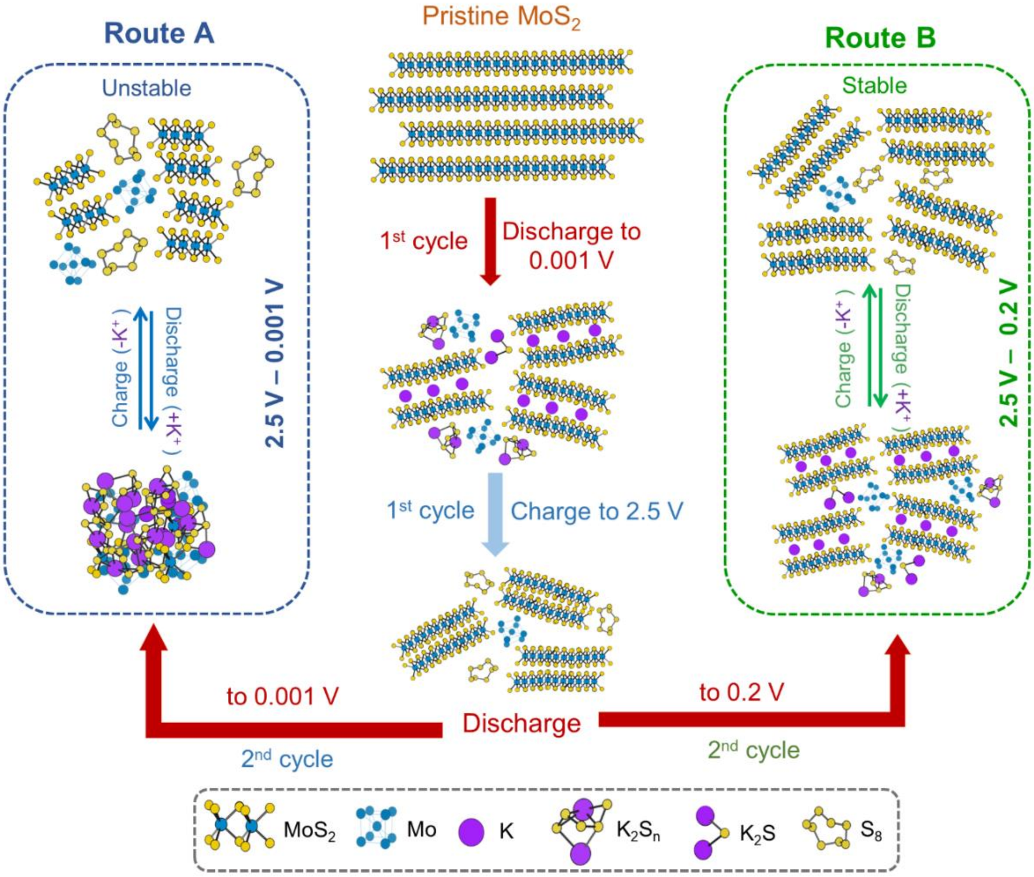

Figure 6. Schematic representation of the mechanism of K-ion storage process in MoS_2 via Routes A and B.

5. Conclusions

In summary, we carried out a mechanistic study on the K storage process in MoS_2 and revealed that Mo and S conversion reactions took place simultaneously during (de)potassiation. The process utilized the cationic redox activity of Mo and anionic redox activity of S simultaneously, which, to the best of our knowledge, was reported for the first time regarding the use of MoS_2 as an anode material for PIBs. Furthermore, we demonstrated the importance of controlling discharge depth in enabling the advantages of dual redox activity. A balance needs to be taken into consideration between maximizing the dual redox activity and minimizing the structural deterioration of MoS_2 and the dissolution of polysulfides. To this end, we showed that it is beneficial to deep discharge to 0.001 V in the initial cycle and raise the discharge depth to 0.2 V from the 2nd cycle onwards, which enhances capacity retention, cycling stability and rate capability compared to consistent deep discharge to 0.001 V. This work does not follow mainstream approaches driven by pursing the high capacity of MoS_2 but takes a deep dive into the underlying electrochemical mechanism of the K storage in MoS_2. We believe our work provides fresh insights into electrochemically storing K-ions in transition metal chalcogenides and an unconventional approach to optimize their PIB performance. We hope our work could shed some light on understanding conversion-type electrode materials of PIBs and contribute to the development of functional materials in research areas outside of energy storage such as catalysis and sensors.d

Acknowledgements

Y.X. acknowledges the support of the Engineering and Physical Sciences Research Council (EP/V000152/1, EP/X000087/1), Leverhulme Trust (RPG-2021-138), and Royal Society (IEC\NSFC\223016). The authors also acknowledge the B18 beamline at Diamond Light Source (DLS) for the allocated experiment session (session ID SP30102-1). For the purpose of open access, the author has applied a Creative Commons Attribution (CC BY) license to any Author Accepted Manuscript version arising.

Conflict of interest

The authors declare no conflict of interest.

References

[1] T. Chowdhury, E. C. Sadler, T. J. Kempa, *Chem. Rev.* **2020**, *120*, 12563.

[2] M. Chhowalla, H. S. Shin, G. Eda, L. J. Li, K. P. Loh, H. Zhang, *Nat. Chem.* **2013**, *5*, 263.

[3] M. Tsai, S. Su, J. Chang, D. Tsai, C. Chen, C. Wu, L. Li, L. Chen, J. He, M. Science, E. Engineering, M. Sciences, M. Sciences, S. Arabia, *ACS Nano* **2014**, *8*, 8317.

[4] E. Storage, Q. Pang, Y. Zhao, Y. Y. Yu, X. Bian, T. B. Schon, B. T. McAllister, P.-F. P. Li, D. S. Seferos, R. Sahoo, A. Pal, T. Pal, *J. Mater. Chem. A* **2017**, *5*, 1.

[5] J. Hu, L. Yu, J. Deng, Y. Wang, K. Cheng, C. Ma, Q. Zhang, W. Wen, S. Yu, Y. Pan, J. Yang, H. Ma, F. Qi, Y. Wang, Y. Zheng, M. Chen, R. Huang, S. Zhang, Z. Zhao, J. Mao, X. Meng, Q. Ji, G. Hou, X. Han, X. Bao, Y. Wang, D. Deng, *Nat. Catal.* **2021**, *4*, 242.

[6] Y. Fan, Z. Yang, W. Hua, D. Liu, T. Tao, M. M. Rahman, W. Lei, S. Huang, Y. Chen, *Adv. Energy Mater.* **2017**, *7*, DOI 10.1002/aenm.201602380.

[7] M. Zhu, X. Du, S. Liu, J. Li, Z. Wang, T. Ono, *J. Mater. Chem. C* **2021**, *9*, 9083.

[8] M. Razeghi, J. Spiece, O. Oğuz, D. Pehlivanoğlu, Y. Huang, A. Sheraz, U. Başçı, P. S. Dobson, J. M. R. Weaver, P. Gehring, T. S. Kasırga, *npj 2D Mater. Appl.* **2023**, *7*, 1.

[9] Y. Wang, L. Yu, X. W. (David) Lou, *Angew. Chemie - Int. Ed.* **2016**, *55*, 7423.

[10] T. Stephenson, Z. Li, B. Olsen, D. Mitlin, *Energy Environ. Sci.* **2014**, *7*, 209.

[11] Y. Wang, J. P. He, H. Q. Pan, Q. P. Wang, L. Zhang, Y. C. Liu, Q. H. Wang, *Rare Met.* **2023**, DOI 10.1007/s12598-023-02447-1.

[12] X. Wei, C. C. Lin, C. Wu, N. Qaiser, Y. Cai, A. Y. Lu, K. Qi, J. H. Fu, Y. H. Chiang, Z. Yang, L. Ding, O. S. Ali, W. Xu, W. Zhang, M. Ben Hassine, J. Kong, H. Y. Chen, V. Tung, *Nat. Commun.* **2022**, *13*, 1.

[13] K. Yao, Z. Xu, M. Ma, J. Li, F. Lu, J. Huang, *Adv. Funct. Mater.* **2020**, *30*, 2001484.

[14] Y. M. Chen, X. Y. Yu, Z. Li, U. Paik, X. W. Lou, *Sci. Adv.* **2016**, *2*, 1.

[15] A. K. Keshari, R. Kumar, *Energy Technol.* **2021**, *9*, 2100179.

[16] T. Kędzierski, K. Wenelska, D. Bęben, B. Zielińska, E. Mijowska, *Electrochim. Acta* **2022**, *434*, 141318.

[17] Y. Teng, H. Zhao, Z. Zhang, Z. Li, Q. Xia, Y. Zhang, L. Zhao, X. Du, Z. Du, P. Lv, K. Świerczek, *ACS Nano* **2016**, *10*, 8526.

[18] L. Chen, Z. Chen, T. Xiang, X. Wang, S. Feng, S. Yang, Z. Wang, Z. Feng, X. Li, J. Huang, *FlatChem* **2023**, *40*, 100520.

[19] J. Yao, Kai; Xu, Zhanwei; Ma, Meng; Li, Jiayin; Lu, Fanyu; Huang, *Adv. Funct. Mater.* **2020**, *30*, 2001484.

[20] Y. Liu, Z. Lei, X. Li, C. Lin, R. Liu, C. Cao, Q. Chen, M. Wei, L. Zeng, Q. Qian, *Dalt. Trans.* **2022**, *51*, 11685.

[21] H. Wang, B. Jia, Z. Zhao, C. Luo, X. Wu, *J. Colloid Interface Sci.* **2022**, *618*, 56.

[22] K. Wu, X. Cao, M. Li, B. Lei, J. Zhan, M. Wu, *Small* **2020**, *16*, 1.

[23] M. Acerce, D. Voiry, M. Chhowalla, *Nat. Nanotechnol.* **2015**, *10*, 313.

[24] W. Kang, Y. Wang, C. An, *New J. Chem.* **2020**, *44*, 20659.

[25] Y. Zhang, L. Zhu, H. Xu, Q. Wu, H. Duan, B. Chen, H. He, *Molecules* **2023**, *28*, DOI 10.3390/molecules28062608.

[26] S. Di, P. Ding, Y. Wang, Y. Wu, J. Deng, L. Jia, Y. Li, *Nano Res.* **2020**, *13*, 225.

[27] X. Jia, Baorui; Yu, Qiyao; Zhao, Yongzhi; Qin, Mingli; Wang, Wei; Liu, Zhiwei; Yen Lao, Cheng; Liu, Ye; Wu, Haowang; Zhang, Zili; Qu, *Adv. Funct. Mater.* **2018**, *28*, 1803409.

[28] Y. Zhong, D. Liu, L. T. Wang, H. guang Zhu, G. Hong, *J. Colloid Interface Sci.* **2020**, *561*, 593.

[29] R. Hu, Y. Fang, K. Zhu, X. Yang, J. Yin, K. Ye, J. Yan, D. Cao, G. Wang, *Appl. Surf. Sci.* **2021**, *564*, 150387.

[30] Y. Cui, L. Zhao, B. Li, W. Feng, T. Cai, X. Li, H. Wang, D. Kong, Z. Fan, L. Zhi, Z. Yan, Q. Xue, W. Xing, *Chem. Eng. J.* **2022**, *450*, 137815.

[31] G. Ma, Y. Zhou, Y. Wang, Z. Feng, J. Yang, *Nano Res.* **2021**, *14*, 3523.

[32] Z. Zhu, S. Xi, L. Miao, Y. Tang, Y. Zeng, H. Xia, Z. Lv, W. Zhang, X. Ge, H. Zhang, J. Wei, S. Cao, J. Chen, Y. Du, X. Chen, *Adv. Funct. Mater.* **2019**, *29*, 1.

[33] W. Choi, Y. S. Choi, H. Kim, J. Yoon, Y. Kwon, T. Kim, J. H. Ryu, J. H. Lee, W. Lee, J. Huh, J. M. Kim, W. S. Yoon, *Chem. Mater.* **2021**, *33*, 1935.

[34] L. Zhang, D. Sun, J. Kang, J. Feng, H. A. Bechtel, L. W. Wang, E. J. Cairns, J. Guo, *Nano Lett.* **2018**, *18*, 1466.

[35] W. Ren, H. Zhang, C. Guan, C. Cheng, *Adv. Funct. Mater.* **2017**, *27*, 1.

[36] X. Du, X. Guo, J. Huang, Z. Lu, H. Tan, J. Q. Huang, Y. Zhu, B. Zhang, *Nanoscale Horizons* **2020**, *5*, 1618.

[37] S. Hao, X. Shen, M. Tian, R. Yu, Z. Wang, L. Chen, *Nano Energy* **2017**, *41*, 217.

[38] K. Wang, W. Hua, Z. Li, Q. Wang, C. Kübel, X. Mu, *ACS Appl. Mater. Interfaces* **2021**, *13*, 40481.

[39] X. Du, X. Guo, J. Huang, Z. Lu, H. Tan, J. Q. Huang, Y. Zhu, B. Zhang, *Nanoscale Horizons* **2020**, *5*, 1618.

[40] B. Xie, Keyu; Yuan, Kai; Li, Xin; Shen,Chao; Liang, Chenglu; Vajtai, Robert; Ajayan, Pulickel; Wei, *Small* **2017**, *13*, 1701471.

[41] J. Zhang, P. Cui, Y. Gu, D. Wu, S. Tao, B. Qian, W. Chu, L. Song, *Adv. Mater. Interfaces* **2019**, *6*, 1.

[42] J. H. Fan, P. Gao, A. M. Zhang, B. R. Zhu, H. L. Zeng, X. D. Cui, R. He, Q. M. Zhang, *J. Appl. Phys.* **2014**, *115*, 053527.

[43] M. Placidi, M. Dimitrievska, V. Izquierdo-Roca, X. Fontané, A. Castellanos-Gomez, A. Pérez-Tomás, N. Mestres, M. Espindola-Rodriguez, S. López-Marino, M. Neuschitzer, V. Bermudez, A. Yaremko, A. Pérez-Rodríguez, *2D Mater.* **2015**, *2*, 035006.

[44] J. Hu, Y. Xie, X. Zhou, Z. Zhang, *ACS Appl. Mater. Interfaces* **2020**, *12*, 1232.

[45] H. Wang, J. Niu, J. Shi, W. Lv, H. Wang, P. A. van Aken, Z. Zhang, R. Chen, W. Huang, *Small* **2021**, *17*, 2102263.

[46] J. Li, B. Rui, W. Wei, P. Nie, L. Chang, Z. Le, M. Liu, H. Wang, L. Wang, X. Zhang, *J. Power Sources* **2020**, *449*, 227481.

[47] X. Ren, Q. Zhao, W. D. McCulloch, Y. Wu, *Nano Res.* **2017**, *10*, 1313.

[48] J. Cui, Yongpeng; Liu, Wei; Feng, Wenting; Zhang, Yuan; Du, Yongxu; Liu, Shuang;

Wang, Huanlei; Chen, Ming; Zhou, *Adv. Funct. Mater.* **2020**, *30*, 1908755.

[49] I. Pudza, D. Bocharov, A. Anspoks, M. Krack, A. Kalinko, E. Welter, A. Kuzmin, *Mater. Today Commun.* **2023**, *35*, 106359.

[50] Y. Zhu, H. Li, Y. Wu, L. Yang, Y. Sun, G. Chen, Y. Liu, Z. Wu, C. Zhang, X. Guo, *RSC Adv.* **2021**, *11*, 28488.

[51] W. Choi, Y. S. Choi, H. Kim, J. Yoon, Y. Kwon, T. Kim, J. H. Ryu, J. H. Lee, W. Lee, J. Huh, J. M. Kim, W. S. Yoon, *Chem. Mater.* **2021**, *33*, 1935.

[52] J. Y. Hwang, H. M. Kim, Y. K. Sun, *J. Mater. Chem. A* **2018**, *6*, 14587.

[53] J. Ding, H. Zhang, W. Fan, C. Zhong, W. Hu, D. Mitlin, *Adv. Mater.* **2020**, *32*, 1.

[54] X. Zhao, Y. Hong, M. Cheng, S. Wang, L. Zheng, J. Wang, Y. Xu, *J. Mater. Chem. A* **2020**, *8*, 10875.

[55] W. Song, X. Yang, T. Zhang, Z. Huang, H. Wang, J. Sun, Y. Xu, J. Ding, W. Hu, *Nat. Commun.* **2024**, *15*, 1005.

[56] C. Nims, B. Cron, M. Wetherington, J. Macalady, J. Cosmidis, *Sci. Rep.* **2019**, *9*, 1.

[57] S. Gu, N. Xiao, F. Wu, Y. Bai, C. Wu, Y. Wu, *ACS Energy Lett.* **2018**, *3*, 2858.

[58] L. Wang, J. Bao, Q. Liu, C. F. Sun, *Energy Storage Mater.* **2019**, *18*, 470.

[59] V. O. Koroteev, S. G. Stolyarova, A. A. Kotsun, E. Modin, A. A. Makarova, Y. V. Shubin, P. E. Plyusnin, A. V. Okotrub, L. G. Bulusheva, *Carbon N. Y.* **2021**, *173*, 194.

[60] X. Fang, C. Hua, X. Guo, Y. Hu, Z. Wang, X. Gao, F. Wu, J. Wang, L. Chen, *Electrochim. Acta* **2012**, *81*, 155.

[61] C. Y. Zhang, C. Zhang, J. L. Pan, G. W. Sun, Z. Shi, C. Li, X. Chang, G. Z. Sun, J. Y. Zhou, A. Cabot, *eScience* **2022**, *2*, 405.